





Cite this: *Phys. Chem. Chem. Phys.*,  
2025, 27, 12248

# Arrangement of $\sigma$ -holes at the halogen atom in halonium cations†

Mariusz Michalczyk \* and Wiktor Zierkiewicz 

Halonium cations are key entities that can stabilize transition states in organocatalysis. The distribution of the electrostatic potential on the crystal structures and theoretical models was investigated in the current study. The Cambridge Structural Database (CSD) survey revealed 478 structures of the  $[L \cdots X \cdots L]^+$  ( $X$  – halogen atom,  $L$  – ligands attached to the halogen) structural motif, which were divided by the values of the  $L \cdots X \cdots L$  angles. The value of this angle determined the number of  $\sigma$ -holes at the halonium cation and hence its ability to accommodate nucleophilic attack. Complexation with HCN as a Lewis base showed that one or two such ligands can be attracted depending on the number of  $\sigma$ -holes. Further investigation into the electrostatic potential distribution on the surface of the model halonium  $[HF_2C_2-X-C_2F_2H]^+$  cations revealed that altering the values of the  $C \cdots X \cdots C$  angles leads to the following consequences: two  $\sigma$ -holes can merge into a single belt-like region, or they may both disappear entirely. The unusual fluctuations in the distribution of  $\sigma$ -holes caused by such geometry maneuvering were observed.

Received 22nd February 2025,  
Accepted 13th May 2025

DOI: 10.1039/d5cp00703h

rsc.li/pccp

## 1. Introduction

Halogen bonds (XBs)<sup>1–5</sup> are the second most well-documented type of noncovalent interactions, following hydrogen bonds (HBs).<sup>6,7</sup> This kind of interaction was officially recognized by the IUPAC<sup>8</sup> in 2013, shortly after its introduction, which appeared in 2005–2007.<sup>4,5,9</sup> The characteristics of XBs are similar to those of hydrogen bonds,<sup>10,11</sup> including the directionality, interaction energy and primary driving force—electrostatics. However, the distinct nature of the halogen bond lies in  $\sigma$ -hole contribution. The “ $\sigma$ -hole”<sup>12–14</sup> expression describes an area of depleted electron density, which can be observed at the outer lobe of the halogen atom (in the position of the partially empty p-orbital) that is covalently bonded with the electron-withdrawing agent. The phenomenon of  $\sigma$ -holes is confirmed not only by theoretical calculations but also by an experiment with Kelvin force probe microscopy.<sup>15</sup> A typical halogen bond is commonly denoted as  $R-X \cdots L$ , where  $R$  is the group covalently attached to the halogen,  $X$  is the halogen atom (usually Cl, Br, or I atoms, rarely a F atom) and  $L$  is a Lewis base (an electron-rich system, *e.g.* an anion) approaching the  $R-X$  molecule. This canonical pattern of halogen bonding has been the focus of research throughout the years, involving both neutral and

anionic complexes.<sup>16–24</sup> Other interactions rationalized in terms of  $\sigma$ -holes are also evidenced in the literature.<sup>25–36</sup> A trend is seen in naming these interactions according to the conventional nomenclature of atomic groups in the periodic table.

Significantly less explored is the involvement of halonium cations in complexes stabilized by halogen bonds, as well as the topic of halonium cations themselves. Only recently (2024), the formation of the 1,3-dibromopropane (DBP<sup>+</sup>) halonium cation was reported in *Nature*.<sup>37</sup> The halogen atom within the halonium cation is able to simultaneously interact with two Lewis bases to form an  $[L \cdots X \cdots L]^+$  specimen. This hypervalent arrangement allows the halogen atom to act as a strong Lewis acid and form halogen bonds with incoming ligands,<sup>38</sup> even those that are highly reluctant to form noncovalent contacts, such as noble gases.<sup>39</sup> Iodonium ion transfer was studied in the theoretical work of Parra within the ternary  $NCI \cdots CH_3I \cdots CN^-$  complex. This trimer was converted to its equivalent form,  $NC^- \cdots CH_3I \cdots NCI$ . The electronic barrier for this conversion has been calculated as 6.44 kcal mol<sup>−1</sup> using the MP2.5 method.<sup>40</sup> Recently, Velasquez *et al.*<sup>41</sup> showed the most important features of many halonium compounds with the  $[N \cdots X \cdots N]^+$  structural motif in the context of theoretical models and structures from the crystal database. The complexes described therein were labeled as three-center-four-halonium compounds, and the nature of the halogen bond was postulated to be more adequately suited to the Pimentel–Rundle<sup>42,43</sup> delocalized molecular orbital model than the untainted electrostatic one. Halonium ions have also been recognized in the literature as potential organocatalysts.

Faculty of Chemistry, Wrocław University of Science and Technology, Wybrzeże  
Wyspiańskiego 27, 50-370 Wrocław, Poland.

E-mail: mariusz.michalczyk@pwr.edu.pl

† Electronic supplementary information (ESI) available. See DOI: <https://doi.org/10.1039/d5cp00703h>



Novikov *et al.* reported that noncovalent interactions involving halonium, chalconium and pniconium cations are responsible for stabilizing the transition state structures in two model reactions: the hydrolysis of methyl chloride and the addition of ammonia to acetone.<sup>44</sup> Likewise, Sysoeva *et al.* reported that halonium and chalconium cations play a role in catalyzing Schiff condensation between 4-methylbenzaldehyde and 2-aminopyridine.<sup>45</sup> The applicability of halonium cations in other organic reactions<sup>46–49</sup> and in designing supramolecular architectures as halogen-bonded organic frameworks (XOF)<sup>50</sup> has been documented elsewhere.

In the present work, our attention is focused on the halonium cation and its molecular electrostatic potential (MEP) distribution. It has been shown<sup>51</sup> that halonium cations have strong acidity due to the anisotropy of the electron density over their surface, resulting in powerful  $\sigma$ -hole region. A guide for recognizing acidity of  $\sigma$ -hole donors is the value of the maximum of electrostatic potential (represented widely in the literature as  $V_{S,max}$ ) measured on the contour of electron isodensity, ordinarily set at 0.001 electrons per Bohr<sup>3</sup>. The MEP for the studied  $Cl^+$ ,  $Br^+$ , and  $I^+$  cations ranged from 256 to 285 kcal mol<sup>−1</sup>, being the greatest for the chloronium cation.<sup>51</sup> It must be stressed that within the neutral hole donors, the  $\sigma$ -hole is positive, even though the surroundings are negatively charged (due to the lone-electron pairs of the halogen atoms). In the ionic halogen  $\sigma$ -hole donors, both the  $\sigma$ -hole and its neighborhood have the same sign; however, in anions, the  $\sigma$ -hole is less negative than the remainder of the surface, while in cations, it is more positive than the vicinity. These distinctive regions are exceptionally prone to nucleophilic attacks. The literature data almost uniformly reveal that the magnitude of the  $\sigma$ -hole in halonium cations is notable (usually more than 100 kcal mol<sup>−1</sup> (ref. 41, 44, 45 and 51)), but a relevant question concerning the number of  $\sigma$ -holes remains: which scenario is more common? One or two  $\sigma$ -holes? According to our previous calculations,<sup>39</sup> for the  $I-Pr^+$  halonium cation ( $Pr$  = propyl entity) there is one  $\sigma$ -hole (as large as 130 kcal mol<sup>−1</sup>), but it is shifted by 5.7° towards the line connecting the  $I$  atom with the midpoint of the  $C-C$  bond (Fig. 1 in the cited work). The location of  $V_{S,max}$  is far from the extensions of two  $C-I$  axes, which is unconventional for halogen-type  $\sigma$ -hole donors. This deviation was even stronger for the  $Cl-Pr^+$  and  $Br-Pr^+$  species. For the halonium cations with a pyridine molecule and  $Xe$  atom, the  $\sigma$ -holes were situated in the standard way, namely, directly along the extension of the  $X-N$  and  $X-Xe$  covalent bond axes, respectively. Then, one can claim that the geometry of the halonium cations affects the distribution of MEP as well as the positioning of the  $\sigma$ -holes. In the current work, a Cambridge Structural Database (CSD)<sup>52</sup> search addresses the question of the number of  $\sigma$ -holes in halonium cations based on the framework of the experimentally obtained structures, whereas theoretical models inspired by CSD-derived compounds made it possible to trace the process of changing the distribution of MEP *versus* slight geometric variations of the halonium cations. Our systematic analysis was aimed at capturing the border geometry of

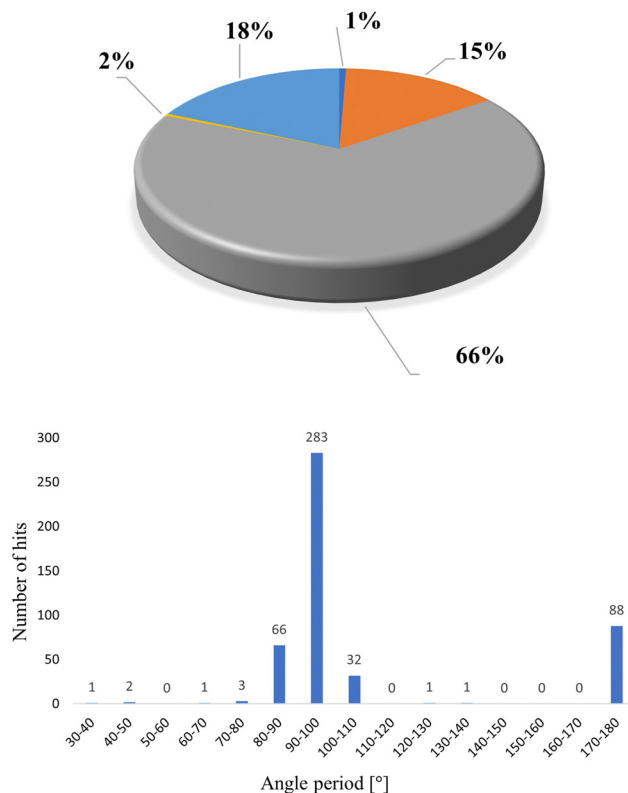


Fig. 1 Pie chart and bar chart representing the distribution of CSD hits in the angular ranges  $[L \cdots X \cdots L']^+$ . Color groups in the pie chart, in order of decreasing abundance: grey, 90–120°, light blue, 150–180°, orange, 60–90°, yellow, 120–150° and dark blue, 30–60°.

halonium cations where the two  $\sigma$ -holes merge into one. The current research could be crucial in understanding the capability of establishing noncovalent interactions by the halonium cations, which is particularly relevant from the point of view of their participation in stabilizing the transition state structures in organocatalysis.

## 2. Computational details

Quantum chemical calculations involving geometry optimization and wave function generation for selected halonium cation models were carried out using the M06-2X method, with the aid of the def2tzvpp<sup>53–56</sup> basis set, by means of the Gaussian 16 (Rev. C.01) code.<sup>57</sup> It was previously stated<sup>37,58–60</sup> that this DFT functional is able to correctly forecast the electronic structure of systems comprising halogen atoms. Its performance has also been validated in benchmark studies.<sup>61,62</sup> Harmonic frequency analysis of normal modes confirmed that the optimized geometries of the model structures are real minima by the absence of any imaginary frequencies. The MEPs for the monomeric systems were calculated using the MultiWFN software (version 3.7)<sup>63,64</sup> to assign the position and magnitude of  $\sigma$ -holes in the investigated halonium compounds. Graphical visualization of the MEP was performed using the VMD 1.9.4 software.<sup>65</sup> The



geometry of the fragments of the crystal structures used within the MEP evaluation was directly taken from the CSD<sup>52</sup> (ver. 5.44) without any pre-optimization. For extra calculations for complexes between halonium cation models adapted from CSD and the HCN molecule as a Lewis base, the full relaxation and interaction energy calculations were performed. The basis set superposition error was reduced in terms of the counterpoise procedure.<sup>66</sup>

## 2.1. The CSD survey and calculations for selected crystalline solids

We surveyed the crystal database aiming to find structures including any halogen atoms of charge +1, bonded to exactly two atoms (L and L'). We considered the value of the  $L \cdots X \cdots L'$  angle as an additional criterion, as the geometry of the  $[L \cdots X \cdots L']^+$  moiety is crucial for the MEP distribution on halonium cations. Such searching was repeated several times by altering the  $L \cdots X \cdots L'$  angle by periods of  $10^\circ$ , starting from the  $30$ – $40^\circ$  range up to the  $170$ – $180^\circ$  compartment. The CSD survey comprised only 3D structures that were non-disordered, with no-errors and  $R$ -factor  $\leq 0.1$  in order to reach the highest possible credibility. The results are presented in Fig. 1 and in Fig. S1–S3 (ESI<sup>†</sup>), while a detailed summary is provided in Table S1 (ESI<sup>†</sup>).

As can be seen in Fig. 1, two thirds of the obtained hits consist of a  $90$ – $120^\circ$   $L \cdots X \cdots L'$  angle motif. In fact, the majority (283 structures) of the revealed hits possess the  $L \cdots X \cdots L'$  angle in a narrow  $90$ – $100^\circ$  range. The second largest group (88 hits) is that with a near-linear geometry of the  $[L \cdots X \cdots L']^+$  group, where the considered angle was close to being half-full. A very small fraction of crystalline solids found were those with tighter packing of the ligands attached to the halogen atom. Angles from  $30^\circ$  to  $80^\circ$  were observed for only seven search results. In the work of Velasquez *et al.*,<sup>41</sup> all the found structures of the  $[N \cdots I \cdots N]^+$  motif had angles from  $175$  to  $180^\circ$ . The CSD survey was refined to provide a more detailed view of the halonium cations available in the CSD. The structures with an iodine atom as the halogen constituted 87% of all found deposited crystals (407 hits), while the remaining hits contained bromine (40), chlorine (18), or fluorine (2) atoms. As for the type of atom with which the ligand binds to the X atom in halonium entities, 73% was carbon, followed by nitrogen (20%). The remaining 7% of found crystals were those with Se, S, O, B, Cu, and Cr atoms (see Fig. S1, ESI<sup>†</sup>). Homo halonium ions (in which X was bound to atoms of the same element) were encountered more frequently than hetero ions (in a ratio of 436 to 31). The distribution of the ligand  $\cdots$  halogen distances ( $L1-X$  and  $L2-X$ ) was represented in the form of a heat plot, as shown in Fig. S2 (ESI<sup>†</sup>). The arrangement of the data points roughly along the diagonal of this figure indicates that the two distances are approximately equal within a particular halonium cation. The highest density of results was in the area corresponding to the  $2.10$ – $2.15$  Å distance, which encompassed about 30% of the surveyed crystals. Analysis of the cell volume in crystalline solids within the CSD revealed that the largest number of hits belonged to the  $1000$ – $2000$  Å<sup>3</sup> compartment. Only a small

fraction of results concerned cells with a volume larger than  $7000$  Å<sup>3</sup> (9 hits out of 467, see Fig. S3, ESI<sup>†</sup>).

Ten selected structures, differing in halogen type, were examined using MEP analysis. The majority (seven out of ten) had the same atoms attached to the halogen atom, which reflects the abovementioned global trend. When the  $L1-X-L2$  angle was  $36$ – $43^\circ$ , only one  $\sigma$ -hole with a magnitude of  $83.2$ – $96.9$  kcal mol<sup>−1</sup> was found on the surface of the molecule. The increase in  $\sigma$ -hole depth followed the order: Cl < Br < I. For the remaining hits, characterized by  $L1-X-L2$  angles from  $91$ – $130^\circ$ , two  $\sigma$ -holes were found. The strength of these holes was nearly equivalent when both ligands were the same, whereas for different ligands a difference in the intensity of the  $\sigma$ -hole was observed. It was up to  $18$  kcal mol<sup>−1</sup> for the AMEPAM structure. Two out of ten molecules, differing considerably in the  $L \cdots X \cdots L$  angle, were chosen for detailed allocation of the electrostatic potential, namely the fragments of the WEVPOC<sup>67</sup> (the iodonium cation of adamantylideneadamantane) and BEVVOR<sup>68</sup> (the gem-difluorovinyl iodonium cation) crystals (marked by bold font in Table S2, ESI<sup>†</sup>). MEP maps for these two compounds are presented in Fig. 2. As both structures are cations of +1 formal charge, the whole examined surface has in fact a positive sign of EP. To differentiate the regions of lower and higher electrostatic potential, color scales have been applied. As depicted in Fig. 2a, part of the WEVPOC<sup>67</sup> structure is characterized by the  $C \cdots I \cdots C$  angle of  $36.0^\circ$ , the lowest of all found in the CSD survey. The MEP protocol unveiled only one  $\sigma$ -hole for this system of magnitude equal to  $96.9$  kcal mol<sup>−1</sup> lying roughly over the midpoint of the C–C bond. For this cation, only one Lewis base is expected to be bound. Conversely, one of the members of the most abundant structural motifs from the CSD search is shown in Fig. 2b.

The fragment of the BEVVOR<sup>68</sup> crystal includes two  $\sigma$ -holes at the halogen atom, on the elongations of the phenyl–I and  $CHCF_2$ –I bonds. They stem from the different arrangement of the  $[C \cdots I \cdots C]^+$  group than in the WEVPOC, as the  $C \cdots I \cdots C$  angle was  $94.7^\circ$ . The maxima of EP within BEVVOR were somewhat different, *viz.*,  $126.1$  and  $132.7$  kcal mol<sup>−1</sup>. A greater  $V_{S,max}$  was found on the extension of the  $CHCF_2$ –I bond. It must

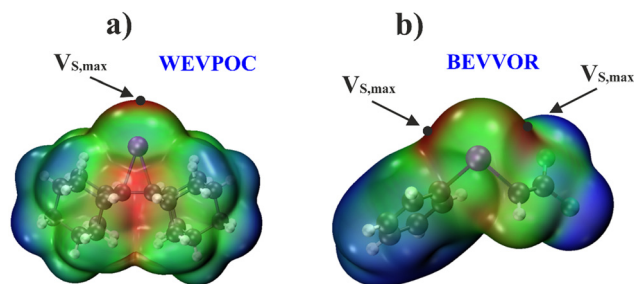


Fig. 2 MEP distribution on the 0.001 electrons per Bohr<sup>3</sup> electron iso-density contour for two fragments of selected halonium cations from CSD: (a) with one  $\sigma$ -hole and (b) with two  $\sigma$ -holes. The color scale is from lower (blue) to higher (red) values of MEP in the following order: (a) from 0.10 to 0.14 a.u., and (b) from 0.12 to 0.20 a.u. Refcodes are taken from CSD. The  $V_{S,max}$  spots are indicated by black dots. Colors of atoms: I – purple, C – grey, H – white, F – cyan.



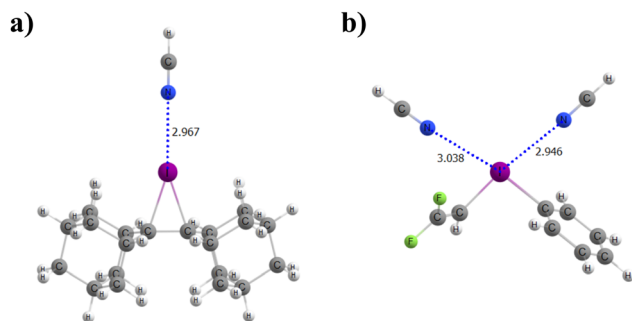


Fig. 3 The DFT optimized structures of the complexes between selected parts of the crystal structures: (a) dimer of WEVPOC with HCN, and (b) trimer BEVVOR with two HCN. Distances in Å.

be stressed that the number and localization of the  $\sigma$ -holes on these two exemplary structures remained the same regardless of the adopted contour of electron density, which was changed from the standard 0.001 electrons per Bohr<sup>3</sup> to ranging from 0.00001 to 0.1 electrons per Bohr<sup>3</sup>.

The two  $\sigma$ -holes located on the BEVVOR system let us assume that it is possible to attach two Lewis bases to such a configuration, giving the BEVVOR hypothetically a capacity of accepting twice as many ligands as the WEVPOC system. To verify this concept, full optimizations of BEVVOR and WEVPOC cation-neutral complexes with one or two HCN ligands (as Lewis bases) were conducted. The resulting complexes are presented in Fig. 3. The two-hole BEVVOR structure was able to host either one or two hydrogen cyanides through one or two  $I \cdots N$  interactions of distance about 3 Å. Both interactions were directed to the  $\sigma$ -hole spots. In the dimer, the HCN molecule was attracted by the area situated around the extension of the  $\text{CHCF}_2\text{-I}$  bond.

The interaction energy for the dimer was  $-13.46 \text{ kcal mol}^{-1}$ . With regard to the trimer, the attachment of two HCN molecules was inequivalent as the  $I \cdots N$  distances were 2.95 and 3.04 Å. A shorter contact was observed on  $\text{CHCF}_2\text{-I}$  bond elongation; so this site had a higher  $V_{S,\text{max}}$  value. The interaction energy was measured in two ways. The interaction energy between two HCN ligands and the cation was  $-25.90 \text{ kcal mol}^{-1}$ , while the  $E_{\text{int}}$  values calculated for each ligand separately were  $-12.11$  and  $-11.37 \text{ kcal mol}^{-1}$ . A more negative value of interaction energy was observed when attaching the HCN ligand on the extension of the difluoroethylene-I bond. A second ligand incorporated into the second  $\sigma$ -hole (less intense by about 5%) sitting on the extension of the phenyl-I bond is bonded weaker by about 6% than the first one. One may ask about the possibility of adding another ligand. We obtained a stable minimum for the tetramer; however, the third ligand located between the previous two was displaced from the halogen atom to a distance of 3.34 Å. The bond path generated by the QTAIM protocol for the bonding of the third ligand is described by the value of electron density ( $\rho$ ) of 0.009 a.u., which is twice as low as for the attachment of the two ligands directed to the  $\sigma$ -hole. The weaker character of bonding a third HCN is also manifested by the value of interaction energy between the single ligand and

the remaining subunits of the system. It is  $-5.81 \text{ kcal mol}^{-1}$  for encompassing a third ligand and  $-9.57$  or  $-10.51 \text{ kcal mol}^{-1}$  for the remaining ones.

In the case of the WEVPOC compound, which was characterized by a single  $\sigma$ -hole, the dyad structure was stabilized by  $I \cdots N$  interaction, which faced the  $\sigma$ -hole with a 2.97 Å distance. The interaction energy of this dimer was  $-9.24 \text{ kcal mol}^{-1}$ , so around 30% weaker bonding than for its BEVVOR counterpart, which is in accordance with the about 25% lower magnitude of the WEVPOC  $\sigma$ -hole. Regarding the trimer, the initial geometry was aligned by putting two ligands on both sides of the  $\sigma$ -hole zone of the iodine atom. The optimization led to complexation with one HCN molecule, which occupied the vicinity of the  $V_{S,\text{max}}$  place at 2.989 Å distance, while the second ligand was repelled outside of the  $\sigma$ -hole spot, to the  $I \cdots N$  distance of 3.579 Å. This value is on the edge of the sum of the van der Waals radii<sup>69</sup> for the respective atoms. The QTAIM analysis for the bonding of the second ligand disclosed two  $\text{H} \cdots \text{N}$  bond paths and one  $I \cdots \text{N}$  bond path, all characterized by  $\rho = 0.007 \text{ a.u.}$  For comparison, the HCN bonded at a shorter distance had  $\rho = 0.017 \text{ a.u.}$  (see Fig. S6, ESI†). The status of gluing a second HCN molecule to the  $\sigma$ -hole in the halonium cation is debatable, as actually, complete dissociation of the second ligand is prevented mostly by the two  $\text{C-H} \cdots \text{N}$  hydrogen bonds. A detailed study on the complexation abilities of halonium cations will be performed in a future project.

## 2.2. Theoretical models

To check the distribution of electrostatic potential around the halogen atom in the halonium cations in detail, three theoretical monomer models based on the BEVVOR crystal structure were designed. The BEVVOR system was reproduced in asymmetric  $[\text{H}_5\text{C}_6\text{-X-C}_2\text{F}_2\text{H}]^+$  molecules ( $\text{X} = \text{Cl}, \text{Br}, \text{or I}$ ), while in the two remaining models we decided to replace the phenyl ring and  $-\text{CHCF}_2$  group to obtain a symmetric arrangement around the X atom, with two identical ligands. Hence, we prepared  $[\text{HF}_2\text{C}_2\text{-X-C}_2\text{F}_2\text{H}]^+$  and  $[\text{H}_5\text{C}_6\text{-X-C}_6\text{H}_5]^+$  system models. These three model systems are illustrated for  $\text{X} = \text{I}$  in Fig. 4.

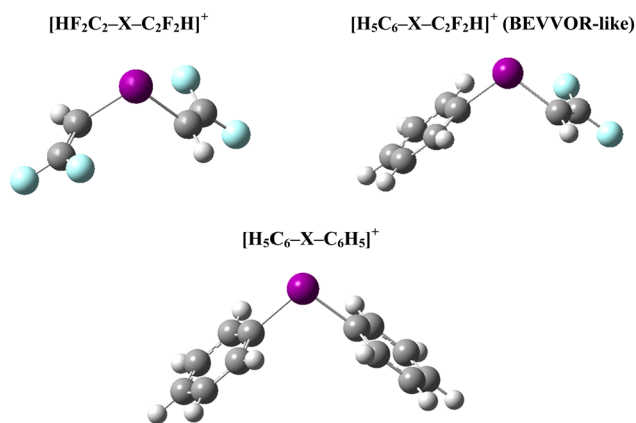


Fig. 4 Iodine representation of three elementary halonium cation models investigated, where  $\text{X} = \text{Cl}, \text{Br}, \text{or I}$ . Colors of atoms: I – purple, C – grey, H – white, F – cyan.





**Table 1** Geometrical parameters and MEP descriptors of the DFT optimized halonium cation models. The C1, C2,  $\alpha$  and  $\beta$  labels are described in Fig. 5. Distances are in Å, angles in degrees, and  $V_{S,max}$  values in kcal mol<sup>-1</sup>

Cationic compounds	$R(C1X)$	$R(C2X)$	$V_{max}(1)$	$V_{max}(2)$	$\alpha$	$\beta$	$\angle C1XV_{max}(1)$	$\angle C2XV_{max}(2)$
HF <sub>2</sub> C <sub>2</sub> -Cl-C <sub>2</sub> F <sub>2</sub> H	1.733	1.733	130.4	130.4	108.0	102.1	173.7	175.9
HF <sub>2</sub> C <sub>2</sub> -Br-C <sub>2</sub> F <sub>2</sub> H	1.880	1.880	132.8	132.8	104.7	106.2	178.5	178.6
HF <sub>2</sub> C <sub>2</sub> -I-C <sub>2</sub> F <sub>2</sub> H (see Fig. 5)	2.050	2.050	136.8	136.8	101.9	106.9	177.0	177.4
H <sub>5</sub> C <sub>6</sub> -Cl-C <sub>2</sub> F <sub>2</sub> H	1.730	1.794	117.1	118.2	103.4	106.8	175.9	179.5
H <sub>5</sub> C <sub>6</sub> -Br-C <sub>2</sub> F <sub>2</sub> H	1.879	1.940	118.4	121.3	103.7	108.4	179.1	175.8
H <sub>5</sub> C <sub>6</sub> -I-C <sub>2</sub> F <sub>2</sub> H	2.054	2.104	121.4	126.0	100.9	111.4	175.6	173.8
H <sub>5</sub> C <sub>6</sub> -Cl-C <sub>6</sub> H <sub>5</sub>	1.786	1.786	107.0	106.9	105.6	106.9	174.0	177.1
H <sub>5</sub> C <sub>6</sub> -Br-C <sub>6</sub> H <sub>5</sub>	1.934	1.934	108.6	108.5	102.2	109.1	177.7	174.8
H <sub>5</sub> C <sub>6</sub> -I-C <sub>6</sub> H <sub>5</sub>	2.103	2.103	111.8	111.8	99.9	110.6	173.7	175.4

The results of full DFT optimization of the studied compounds are gathered in Table 1. In Fig. 5, in turn, there is a MEP map for one of the deliberated structures – [HF<sub>2</sub>C<sub>2</sub>-I-C<sub>2</sub>F<sub>2</sub>H]<sup>+</sup>, where all descriptors appearing in Table 1 are explained. For all the monomers studied, two holes were identified on the halonium cation surfaces, as it was in the case of the original crystal source. The values of  $V_{S,max}$  were all above 100 kcal mol<sup>-1</sup>, which is consistent with earlier literature reports.<sup>41,44,45,51</sup> Notably, the  $\sigma$ -hole magnitudes are in the order Cl < Br < I, which is in line with the lower electronegativity and greater polarizability of the heavier halogen atoms. The C1-X distances were sorted in the same manner, from lighter to heavier halogens. Within the three main model groups, the most intense  $\sigma$ -holes can be found for the [HF<sub>2</sub>C<sub>2</sub>-X-C<sub>2</sub>F<sub>2</sub>H]<sup>+</sup> group (from 130.4 to 136.8 kcal mol<sup>-1</sup>), followed by the [H<sub>5</sub>C<sub>6</sub>-X-C<sub>2</sub>F<sub>2</sub>H]<sup>+</sup> collection (maxima of EP in the range of 117.1 to 126.0 kcal mol<sup>-1</sup>) and [H<sub>5</sub>C<sub>6</sub>-X-C<sub>6</sub>H<sub>5</sub>]<sup>+</sup> set, where the  $V_{S,max}$  values were below 112 kcal mol<sup>-1</sup>. As was expected, for the symmetric compounds, the electrostatic potentials of both holes were identical, while for the asymmetric [H<sub>5</sub>C<sub>6</sub>-X-C<sub>2</sub>F<sub>2</sub>H]<sup>+</sup> models, there were differences in the  $\sigma$ -hole magnitudes of the values from 1 to 5 kcal mol<sup>-1</sup>, deepening with the increase in the atomic size of X. In more detail, a higher  $V_{S,max}$  was found on the extension of the CHCF<sub>2</sub>-X bond, which agrees with the higher electron-withdrawing character of the difluoroethylene group, as well as the results obtained for the BEVVOR crystal structure. The  $\alpha$  and  $\beta$  tags were introduced to signpost the C1-X-C2 and  $V_{max}(2)$ -X- $V_{max}(1)$  angles, which are crucial in further studies where the geometry of the halonium cation will be modified. It should be underlined that these angles do not correspond to apical positions. For the [H<sub>5</sub>C<sub>6</sub>-X-C<sub>2</sub>F<sub>2</sub>H]<sup>+</sup> and [H<sub>5</sub>C<sub>6</sub>-X-C<sub>6</sub>H<sub>5</sub>]<sup>+</sup>

cations,  $\beta$  was bigger than  $\alpha$ , while the reverse was true only for the [HF<sub>2</sub>C<sub>2</sub>-Cl-C<sub>2</sub>F<sub>2</sub>H]<sup>+</sup> molecules. These differences are explained by the last two columns of Table 1. They collected the values of the C1/C2-X- $V_{max}(1)$ / $V_{max}(2)$  angles as a measure of the location of the  $\sigma$ -hole towards the extension of the given bond. For a perfectly linear  $\sigma$ -hole assembly, these values should be equal to 180°. According to our results, none of them were 180°, regardless of whether the surroundings of the X atoms were identical or not. The deviations from linearity were in the range of 0.5 to 6.3 degrees, with no systematic trends concerning specific X atoms or the remainder of the cation. Consequently, deviation from linearity in the layout of  $\sigma$ -holes triggered the inequality of the  $\alpha$  and  $\beta$  angles.

To evaluate the behavior of the  $\sigma$ -hole setting in the halonium cations for various geometries, the three models with the boldest  $\sigma$ -holes in each group (with X = I) were considered for a detailed study. In Table 2, the geometrical data of  $\sigma$ -hole positioning when the  $\alpha$  angle was increased and decreased in 10° intervals for the [HF<sub>2</sub>C<sub>2</sub>-I-C<sub>2</sub>F<sub>2</sub>H]<sup>+</sup> cation are summarized. Changes introduced to the equilibrium geometry caused expected worsening of the total electronic energies, which is shown in the last column of Table 2. In the extreme cases, the total electronic energy was worse than for the fully relaxed compound by about 50 kcal mol<sup>-1</sup>. The equivalent results for the [H<sub>5</sub>C<sub>6</sub>-I-C<sub>2</sub>F<sub>2</sub>H]<sup>+</sup> and [H<sub>5</sub>C<sub>6</sub>-I-C<sub>5</sub>H<sub>6</sub>]<sup>+</sup> cations are listed in Tables S3 and S4 (ESI†). The outcomes obtained provide unusual trends. When the  $\alpha$  angle (C1-X-C2) is enlarged, the  $\beta$  angle ( $V_{max}(2)$ -X- $V_{max}(1)$ ) simultaneously diminishes from 106.9° at the equilibrium geometry to 88.1°. This change is accompanied by the lowering of the  $\sigma$ -hole magnitude (from 136.8 to 118.9 kcal mol<sup>-1</sup>) and continued deviation of the  $\sigma$ -hole location from linearity as the C-X- $V_{max}$  angles drop from about 177° to 152–153°. Thus, spreading the position of the identical ligands attached to the I atom does not spread the position of the  $\sigma$ -holes (as could be predicted), but brings them closer together. When  $\alpha = 151.9^\circ$ ,  $V_{S,max}$  values are no longer detected at the former placements as the potential became flattened around the halogen atom. Conversely, when both the -CF<sub>2</sub>H<sub>2</sub> substituents are pulled towards each other by decreasing  $\alpha$  angle, a corresponding decrease in the  $\beta$  angle can be expected. However, the behavior of  $\beta$  is inverted—its value rises from 106.9° to 119.6° for  $\alpha = 71.9^\circ$ , then stabilizes for  $\alpha = 61.9^\circ$ . At the same time, the  $\sigma$ -hole power is enhanced, whereas the  $\sigma$ -hole digression from the linear arrangement along the I-CF<sub>2</sub>H<sub>2</sub>

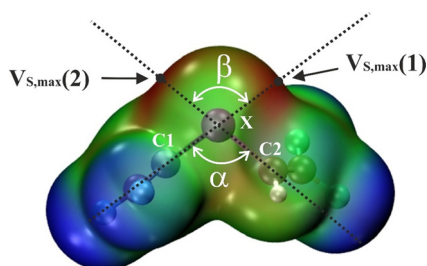


**Fig. 5** MEP distribution on the 0.001 electrons per Bohr<sup>3</sup> electron iso-density contour for the [HF<sub>2</sub>C<sub>2</sub>-I-C<sub>2</sub>F<sub>2</sub>H]<sup>+</sup> molecule. The color scale is from 0.12 a.u. (blue) to 0.22 a.u. (red). The  $V_{S,max}$  spots are indicated by black dots. Colors of atoms: I – purple, C – grey, H – white, F – cyan.



**Table 2** Geometrical parameters describing the  $\sigma$ -hole location of the  $[\text{HF}_2\text{C}_2-\text{I}-\text{C}_2\text{F}_2\text{H}]^+$  model. Values for the equilibrium geometry are in bold. The  $V_{\text{S,max}}$  in  $\text{kcal mol}^{-1}$ , angles in degrees, and energies in  $\text{kcal mol}^{-1}$

Compound	$\alpha$	$\beta$	$V_{\text{S,max}}(1)$	$V_{\text{S,max}}(2)$	$\angle \text{C1XV}_{\text{S,max}}(1)$	$\angle \text{C2XV}_{\text{S,max}}(2)$	Total electronic energy (in relation to equilibrium geometry)
$[\text{HF}_2\text{C}_2-\text{I}-\text{C}_2\text{F}_2\text{H}]^+$	151.9	—	—	—	—	—	52.38
	141.9	88.1	118.9	118.9	152.8	152.0	37.70
	131.9	92.1	123.7	123.7	159.8	160.3	14.54
	121.9	97.0	128.4	128.4	167.3	167.6	6.72
	111.9	103.4	132.7	132.7	174.2	175.6	1.76
	<b>101.9</b>	<b>106.9</b>	<b>136.8</b>	<b>136.8</b>	<b>177.0</b>	<b>177.4</b>	<b>0.00</b>
	91.9	111.9	140.3	140.3	171.3	168.5	1.95
	81.9	116.3	143.3	143.3	162.1	163.4	8.44
	71.9	119.6	144.9	144.9	156.4	155.8	20.71
	61.9	119.4	141.0	141.0	152.5	149.9	39.48
	59.9	94.4	138.4	138.2	175.4	150.6	43.81
	57.9	—	138.7 <sup>a</sup>	—	153.1	149.0 <sup>b</sup>	48.25

<sup>a</sup> Only one  $\sigma$ -hole exists. <sup>b</sup>  $\angle \text{C2-X-V}_{\text{S,max}}(1)$ .

axes rapidly grows. Therefore, further reduction of  $\alpha$  was performed in smaller steps, specifically at  $2^\circ$  intervals. Starting from  $\alpha = 59.9^\circ$ ,  $\beta$  shrinks by  $25^\circ$  and when  $\alpha$  reaches  $57.9^\circ$ , two  $\sigma$ -holes are merged into one. The integration of the  $\sigma$ -holes is confirmed for  $\alpha = 57.9^\circ$  on the various electron isodensities (0.005, 0.001, 0.01, and 0.05 electrons per Bohr<sup>3</sup>). The trajectory of the change in  $\beta$  angle *versus*  $\alpha$  angle is highlighted in Fig. 6. Roughly the same pattern was observed for the  $[\text{H}_5\text{C}_6-\text{I}-\text{C}_2\text{F}_2\text{H}]^+$  and  $[\text{H}_5\text{C}_6-\text{I}-\text{C}_5\text{H}_6]^+$  cations (see Tables S3 and S4 along with Fig. S4 and S5, ESI<sup>†</sup>). It is worth mentioning that the  $V_{\text{S,max}}$  for the merged  $\sigma$ -hole is not the sum of the two precedent  $\sigma$ -holes but is comparable to their individual magnitudes ( $138.7 \text{ kcal mol}^{-1}$ ). This could be explained based on the formula for calculating  $V_{\text{S,max}}$ .<sup>51</sup> Its value depends not only on the electron density of the system but also on the contribution of the nuclei. The fused  $\sigma$ -hole operates on the same electron density and nuclei contribution as their earlier “versions”. Based on the aforementioned results deforming the halonium cation beyond its equilibrium geometry results in changes that can cause two  $\sigma$ -holes merge into one or even result in their complete disappearance. The geometry of the  $\sigma$ -hole sites as the  $\alpha$  angle changes is counterintuitive, as narrowing the distance between the ligands bound to the X atom pushes the

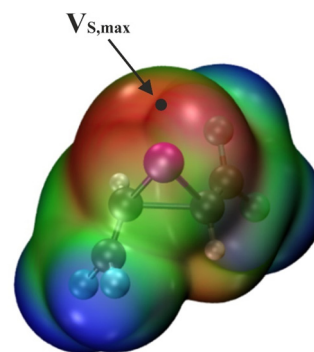


**Fig. 7** MEP distribution on the 0.001 electrons per Bohr<sup>3</sup> electron isodensity contour for the  $[\text{HF}_2\text{C}_2-\text{I}-\text{C}_2\text{F}_2\text{H}]^+$  molecule when  $\alpha = 57.9^\circ$ . Color scale is from 0.12 a.u. (blue) to 0.22 a.u. (red). The  $V_{\text{S,max}}$  spot is indicated by a black dot. Colors of atoms: I – purple, C – grey, H – white, F – cyan.

$\sigma$ -holes apart, while in contrast, increasing the distance between these ligands pulls the  $\sigma$ -holes closer together. This anomaly could be explained by the fact that ligand tightening associated with the halogen atom (lowering values of  $\alpha$ ) might relocate the electron density above that atom, causing  $\sigma$ -hole regions to form farther away rather than near it. When we open the gap between the ligands (rising  $\alpha$  values), the electron density occupies that region, thereby allowing the  $\sigma$ -holes above the halogen atom to be closer together.

Fig. 7 answers the question of how this conjoined  $\sigma$ -hole region appears. The new, deformed hole is represented by the broad belt of electrostatic potential (colored in red on Fig. 7) of values higher than the remaining part of the molecule. The  $V_{\text{S,max}}$  is centered over the I atom at the distance of  $2.125 \text{ \AA}$  from it.

### 3. Conclusions

The analysis of the distribution of the electrostatic potential over selected halonium cations has been carried out. The presence of one or two  $\sigma$ -holes at the halogen atom of the halonium cation decides how many ligands can be attached to the given system, which might be crucial for its functionality in

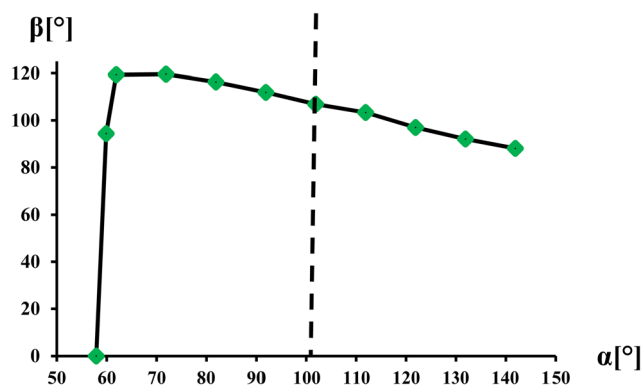


**Fig. 6** Chart representing the changes of  $\beta$  angle *versus*  $\alpha$  angle in the  $[\text{HF}_2\text{C}_2-\text{I}-\text{C}_2\text{F}_2\text{H}]^+$  model. The dashed line designates equilibrium geometry.



organic catalysis as a carrier of transition state structures. The number of  $\sigma$ -holes is a direct consequence of the alignment of the  $[L \cdots X \cdots L]^+$  moiety. Among the crystalline solids revealed by the CSD survey, two of significantly different  $L \cdots X \cdots L$  angles may epitomize different Lewis base binding capacities. Within the current project, it has been demonstrated that the amount of  $\sigma$ -holes on the halonium cations determined whether they are able to accept one or two HCN ligands. Based on the CSD content, the more common scenario is when two  $\sigma$ -holes are presented, as the values of the  $L \cdots X \cdots L$  angles mainly accumulated within the 90–120° range. When this angle is manipulated within halonium cations, two effects may emerge:  $\sigma$ -holes can be merged into one (by decreasing this angle by about 40°) or both of them may be reduced to an area of levelled positive EP (by increasing this angle by about 50°). An explanation of the unusual behavior of the  $\sigma$ -hole positioning relative to each other between these two border cases has been proposed.

## Data availability

The data supporting this article have been included as part of the ESI.†

## Conflicts of interest

There are no conflicts to declare.

## Acknowledgements

The authors gratefully acknowledge Wrocław Center for Networking and Supercomputing (WCSS). This work was financed by a statutory activity subsidy from the Polish Ministry of Science and Higher Education for the Faculty of Chemistry of Wrocław University of Science and Technology.

## References

- P. Politzer, J. S. Murray and T. Clark, *Phys. Chem. Chem. Phys.*, 2013, **15**, 11178–11189.
- P. Politzer and J. S. Murray, *ChemPhysChem*, 2013, **14**, 278–294.
- P. Politzer, K. E. Riley, F. A. Bulat and J. S. Murray, *Comput. Theor. Chem.*, 2012, **998**, 2–8.
- P. Politzer, P. Lane, M. C. Concha, Y. G. Ma and J. S. Murray, *J. Mol. Model.*, 2007, **13**, 305–311.
- T. Clark, M. Hennemann, J. S. Murray and P. Politzer, *J. Mol. Model.*, 2007, **13**, 291–296.
- S. Scheiner, *Hydrogen Bonding: A Theoretical Perspective*, Oxford University Press, New York, 1997.
- G. A. Jeffrey and G. A. Jeffrey, *An introduction to hydrogen bonding*, Oxford university press, New York, 1997.
- G. R. Desiraju, P. S. Ho, L. Kloo, A. C. Legon, R. Marquardt, P. Metrangolo, P. Politzer, G. Resnati and K. Rissanen, *Pure Appl. Chem.*, 2013, **85**, 1711–1713.
- T. Clark, M. Hennemann, J. S. Murray and P. Politzer, *J. Mol. Model.*, 2007, **13**, 291–296.
- S. J. Grabowski, *Phys. Chem. Chem. Phys.*, 2013, **15**, 7249–7259.
- P. Metrangolo and G. Resnati, *Science*, 2008, **321**, 918–919.
- P. Politzer, J. S. Murray and T. Clark, *Top. Curr. Chem.*, 2015, **358**, 19–42.
- J. S. Murray, P. Lane, T. Clark, K. E. Riley and P. Politzer, *J. Mol. Model.*, 2012, **18**, 541–548.
- J. S. Murray, P. Lane and P. Politzer, *J. Mol. Model.*, 2009, **15**, 723–729.
- B. Mallada, A. Gallardo, M. Lamanec, B. de la Torre, V. Spirko, P. Hobza and P. Jelinek, *Science*, 2021, **374**, 863.
- I. Alkorta, J. Elguero and A. Frontera, *Crystals*, 2020, **10**, 180.
- L. H. E. Wieske and M. Erdelyi, *J. Am. Chem. Soc.*, 2024, **146**, 3–18.
- S. Burguera, R. M. Gomila, A. Bauzá and A. Frontera, *Inorganics*, 2023, **11**, 80.
- S. Scheiner, *J. Phys. Chem. A*, 2022, **126**, 6443–6455.
- I. Benito, R. M. Gomila and A. Frontera, *CrystEngComm*, 2022, **24**, 4440–4446.
- S. M. Zhang, J. H. Cheng, H. J. Cao, M. J. Ma, C. Li, X. Y. Song and Z. M. Zhou, *Chem. Commun.*, 2025, **61**, 2500–2503.
- Z. J. Liang, F. D. Dong, L. Ye, K. Zheng, D. Y. Hu, X. Feng, W. Y. Su, Z. S. Wang, M. Y. Zhou, Z. L. Fang, D. D. Zhou, J. P. Zhang and X. M. Chen, *Chem. Sci.*, 2025, **7**, 3307–3312.
- S. R. S. Gudimetla, P. K. Subramaniyan, S. G. Subramaniapillai, S. V. Buddha, O. Blacque, M. J. Percino and S. Thamotharan, *J. Mol. Struct.*, 2025, **1326**, 141165.
- A. Frontera and S. Emamian, *J. Phys. Chem. A*, 2025, **5**, 1368–1385.
- Q. Z. Wu, S. A. C. McDowell and Q. Z. Li, *Appl. Organomet. Chem.*, 2023, **37**, e7052.
- P. Middya, M. Karmakar, R. M. Gomila, M. G. B. Drew, A. Frontera and S. Chattopadhyay, *New J. Chem.*, 2023, **47**, 9346–9363.
- I. M. Garazade, A. V. Gurbanov, R. M. Gomila, A. Frontera, A. V. M. Nunes, K. T. Mahmudov and A. J. L. Pombeiro, *New J. Chem.*, 2023, **47**, 15856–15861.
- S. Burguera, A. Frontera and A. Bauza, *Inorg. Chem.*, 2023, **62**, 6740–6750.
- G. Resnati, A. Pizzi and M. Calabrese, *Acta Crystallogr., Sect. A: Found. Adv.*, 2022, **78**, E200.
- R. M. Gomila and A. Frontera, *Molecules*, 2022, **27**, 6597.
- A. Pizzi, A. Daolio, M. Calabrese, G. Terraneo, A. Frontera and G. Resnati, *Acta Crystallogr., Sect. A: Found. Adv.*, 2021, **77**, C800.
- M. Michalczyk, W. Zierkiewicz and S. Scheiner, *Phys. Chem. Chem. Phys.*, 2024, **26**, 5836–5847.
- R. Beccaria, A. Dhaka, M. Calabrese, A. Pizzi, A. Frontera and G. Resnati, *Chem. – Eur. J.*, 2024, **30**, e202303641.
- N. Liu, Z. Han, Y. Lu, Z. Xu, W. Zhu and H. Liu, *Chem. Phys.*, 2024, **576**, 112113.
- S. Scheiner, *ChemPhysChem*, 2023, e202200936.
- K. T. Mahmudov, A. V. Gurbanov, V. A. Aliyeva, M. F. C. Guedes da Silva, G. Resnati and A. J. L. Pombeiro, *Coord. Chem. Rev.*, 2022, **464**, 214556.



- 37 J. Heo, D. Kim, A. Segalina, H. Ki, D. S. Ahn, S. Lee, J. Kim, Y. Cha, K. W. Lee, J. Yang, J. P. F. Nunes, X. Wang and H. Ihee, *Nature*, 2024, **625**, 710–714.
- 38 L. Turunen and M. Erdélyi, *Chem. Soc. Rev.*, 2020, **49**, 2688–2700.
- 39 W. Zierkiewicz, S. Scheiner and M. Michalczyk, *Phys. Chem. Chem. Phys.*, 2024, **26**, 25762–25766.
- 40 R. D. Parra, *J. Mol. Model.*, 2024, **30**, 363.
- 41 J. D. Velasquez, J. Echeverría and S. Alvarez, *Inorg. Chem.*, 2023, **62**, 8980–8992.
- 42 G. C. Pimentel, *J. Chem. Phys.*, 1951, **19**, 446–448.
- 43 R. E. Rundle, *J. Am. Chem. Soc.*, 1947, **69**, 1327–1331.
- 44 A. S. Novikov and D. S. Bolotin, *Org. Biomol. Chem.*, 2022, **20**, 7632–7639.
- 45 A. A. Sysoeva, Y. V. Safinskaya, M. V. Il'in, A. S. Novikov and D. S. Bolotin, *Org. Biomol. Chem.*, 2025, **8**, 1970–1980.
- 46 S. Oishi, T. Fujinami, Y. Masui, T. Suzuki, M. Kato, N. Ohtsuka and N. Momiyama, *Science*, 2022, **25**, 105220.
- 47 M. Kaasik and T. Kanger, *Front. Chem.*, 2020, **8**, 599064.
- 48 K. Takagi, H. Murakata and T. Hasegawa, *Macromolecules*, 2022, **55**, 5756–5765.
- 49 L. Racicot and M. A. Ciufolini, *ARKIVOC*, 2024, **2**, 202312127.
- 50 G. Gong, F. Xie, L. Wang, J. Wang and S. Chen, *Synlett*, 2022, 423–428.
- 51 P. Ramasami and J. S. Murray, *J. Mol. Model.*, 2024, **30**, 81.
- 52 C. R. Groom, I. J. Bruno, M. P. Lightfoot and S. C. Ward, *Acta Crystallogr., Sect. B: Struct. Sci., Cryst. Eng. Mater.*, 2016, **72**, 171–179.
- 53 F. Weigend, *Phys. Chem. Chem. Phys.*, 2006, **8**, 1057–1065.
- 54 F. Weigend and R. Ahlrichs, *Phys. Chem. Chem. Phys.*, 2005, **7**, 3297–3305.
- 55 Y. Zhao and D. G. Truhlar, *Acc. Chem. Res.*, 2008, **41**, 157–167.
- 56 Y. Zhao and D. G. Truhlar, *Theor. Chem. Acc.*, 2008, **120**, 215–241.
- 57 M. J. Frisch, G. W. Trucks, H. B. Schlegel, G. E. Scuseria, M. A. Robb, J. R. Cheeseman, G. Scalmani, V. Barone, G. A. Petersson, H. Nakatsuji, X. Li, M. Caricato, A. V. Marenich, J. Bloino, B. G. Janesko, R. Gomperts, B. Mennucci, H. P. Hratchian, J. V. Ortiz, A. F. Izmaylov, J. L. Sonnenberg, F. Williams, F. Ding, F. Lipparini, F. Egidi, J. Goings, B. Peng, A. Petrone, T. Henderson, D. Ranasinghe, V. G. Zakrzewski, J. Gao, N. Rega, G. Zheng, W. Liang, M. Hada, M. Ehara, K. Toyota, R. Fukuda, J. Hasegawa, M. Ishida, T. Nakajima, Y. Honda, O. Kitao, H. Nakai, T. Vreven, K. Throssell, J. A. Montgomery, Jr., J. E. Peralta, F. Ogliaro, M. J. Bearpark, J. J. Heyd, E. N. Brothers, K. N. Kudin, V. N. Staroverov, T. A. Keith, R. Kobayashi, J. Normand, K. Raghavachari, A. P. Rendell, J. C. Burant, S. S. Iyengar, J. Tomasi, M. Cossi, J. M. Millam, M. Klene, C. Adamo, R. Cammi, J. W. Ochterski, R. L. Martin, K. Morokuma, O. Farkas, J. B. Foresman and D. J. Fox, *Gaussian 16 Rev. C.01*, Wallingford, CT, 2016.
- 58 M. V. Il'in, A. A. Sysoeva, A. S. Novikov and D. S. Bolotin, *J. Org. Chem.*, 2022, **87**, 4569–4579.
- 59 N. Mehta, T. Fellowes, J. M. White and L. Goerigk, *J. Chem. Theory Comput.*, 2021, **17**, 2783–2806.
- 60 S. N. Yunusova, D. S. Bolotin, M. A. Vovk, P. M. Tolstoy and V. Y. Kukushkin, *Eur. J. Org. Chem.*, 2020, 6763–6769.
- 61 A. Bauza, I. Alkorta, A. Frontera and J. Elguero, *J. Chem. Theory Comput.*, 2013, **9**, 5201–5210.
- 62 N. Mardirossian and M. Head-Gordon, *J. Chem. Theory Comput.*, 2016, **12**, 4303–4325.
- 63 T. Lu and F. Chen, *J. Mol. Graphics Modell.*, 2012, **38**, 314–323.
- 64 T. Lu and F. Chen, *J. Comput. Chem.*, 2012, **33**, 580–592.
- 65 W. Humphrey, A. Dalke and K. Schulten, *J. Mol. Graphics Modell.*, 1996, **14**, 33–38.
- 66 S. F. Boys and F. Bernardi, *Mol. Phys.*, 1970, **19**, 553–566.
- 67 R. S. Brown, R. W. Nagorski, A. J. Bennet, R. E. D. McClung, G. H. M. Aarts, M. Klobukowski, R. McDonald and B. D. Santarsiero, *J. Am. Chem. Soc.*, 1994, **116**, 2448–2456.
- 68 C. Ge, B. Wang, Y. Jiang and C. Chen, *Commun. Chem.*, 2022, **5**, 167.
- 69 S. Alvarez, *Dalton Trans.*, 2013, **42**, 8617–8636.

